

Research Summary

Bo Li

October 2009

My research focuses on applied aspects of the calculus of variations and partial differential equations, particularly nonlinear equations arising from physics and chemistry, and numerical analysis and scientific computing, particularly finite-element analysis and numerical methods for interface motion. I have worked on mathematical and numerical problems arising from materials science, such as those of martensitic microstructure and epitaxial growth of crystalline thin films, and from biochemistry and biophysics, such as those of molecular solvation, electrostatics, and biological pattern formation. In what follows, I summarize my research accomplishments and list my publications.

1 Superconvergence in Finite-Element Methods

Let V be a space of functions and $u \in V$ the solution of an elliptic boundary-value problem. Let V_h be a finite-element space containing all piecewise polynomials of degree up to $k \geq 1$ and $u_h \in V_h$ the finite-element approximation of u , where h is the mesh size. Standard optimal error estimates provide

$$\|u - u_h\| = O(h^{k+1}) \quad \text{and} \quad \|\nabla u - \nabla u_h\| = O(h^k) \quad \text{as } h \rightarrow 0,$$

where $\|\cdot\|$ is the L^2 or L^∞ norm. However, practical computations often show higher-order convergence

$$|u(z_h) - u_h(z_h)| = O(h^{k+2}) \quad \text{or} \quad |\nabla u(z_h) - \bar{\nabla} u_h(z_h)| = O(h^{k+1}) \quad \text{as } h \rightarrow 0$$

on a set of discrete points z_h , e.g., the finite-element nodal points, where $\bar{\nabla}$ is the gradient averaged from neighboring elements. This is superconvergence. Its study began in the early 1970's.

1.1 Superconvergence for nonconforming finite elements

By the early 1980's, superconvergence had been proved only for some conforming ($V_h \subset V$) finite elements. The mathematical justification of the superconvergence for nonconforming finite elements ($V_h \not\subset V$), however, remained open for many years. In 1987, I first solved this open problem for the Wilson nonconforming finite element in a special setting.¹ My idea was to decompose the nonconforming approximation into a conforming part known to be superconvergent and a nonconforming part of high order. In [2], Chen and I studied the general case. Besides superconvergence, we also obtained the solution expansion and lower bounds in negative norms for the solution error. Our results indicated that the Wilson element is asymptotically not better than the conforming bilinear element.

In [3], my collaborators and I proved the superconvergence for the rotated trilinear finite elements, a class of nonconforming finite elements that had been applied to the Stokes problem modeling incompressible fluids and nonconvex variational problems modeling crystalline microstructure.

1.2 Superconvergence for conforming simplicial finite elements

For a conforming finite element, the superconvergence was traditionally proved in three steps: (1) identify superconvergence points for the Lagrange interpolation $I_h u$; (2) establish a higher-order "weak energy estimate" for the underlying bilinear form $a : V \times V \rightarrow \mathbb{R}$, often via the cancellation of contributions from neighboring elements,

$$|a(u - I_h u, v_h)| \leq Ch^{k+1} \|\nabla v_h\|_{L^2} \quad \forall v_h \in V_h, \quad (1.1)$$

¹This work was first reported in the Chinese First National Conference on Numerical Solutions of Partial Differential Equations in 1987 and then collected in the book *Superconvergence Theory of Finite-Element Methods* (in Chinese), by Qiding Zhu and Qun Lin, Hunan Science Press, 1989.

where $C > 0$ a constant independent of h ; and (3) replace v_h in the above inequality by the finite-element Green's function and estimate its norm. In the early 1980's, the key estimate (1.1) was established for rectangular elements, and linear ($k = 1$) and quadratic ($k = 2$) triangular elements.

Is the estimate (1.1) still true for a triangular finite element of higher order $k \geq 3$? In 1989, I constructed counterexamples to give a negative answer to this question for $k = 3$, and proved that the Lagrange interpolation points and the superconvergence points for the finite-element solution are not identical [1]. These results were confirmed numerically by Babuska *et al.* (Numer. Methods for PDEs, 12, 347–392, 1996). The essential idea in my construction was to use a “bubble” finite-element test function $v_h \in V_h$ which vanishes on all element edges, making it impossible for the technique of cancellation to work. Such a bubble function exists only if there is an interior node, which is not true for $k = 1, 2$. Fifteen years later, in [15], I extended my work to any degree k and any space dimension $d \geq 2$ that satisfy the condition $k \geq d + 1$ for the existence of an interior node.

Questioning the generality of the traditional approach to superconvergence, my work [1] received much attention. It was cited as “a little known but in my opinion important paper” in: L. B. Wahlbin, Superconvergence in Galerkin Finite Element Methods, Springer, 1995 (cf. Section 7.4). In fact, my work [1] motivated the development of a new and more general, symmetry-based approach to superconvergence by Schatz, Sloan, and Wahlbin (SIAM J. Numer. Anal., 33, 505–521, 1996).

1.3 Superconvergence patch recovery technique

In 1992, Zienkiewicz and Zhu developed by numerical experiment a superconvergence patch recovery technique (cf. [8] for the references). In [8], Zhang and I gave a rigorous justification of this technique.

2 Variational Models of Martensitic Microstructure

A martensitic crystal such as a shape-memory alloy has a symmetric lattice structure known as austenite that is stable at a high temperature and several less symmetric lattice structures known as martensite or martensitic variants that are equally stable at a low temperature. Upon changing temperature or applying stress, such a crystal undergoes a reversible phase transformation between the austenite and martensite or between the martensitic variants. The lattice changes from the austenite to martensitic variants, assuming N of them, are described by transformation matrices U_1, \dots, U_N , cf. Fig. 2.1 (left). During such a transformation, a fine-scale mixture of coherent martensitic variants appears. This is martensitic microstructure. It enables a martensitic crystal to recover its strain and change its shape.

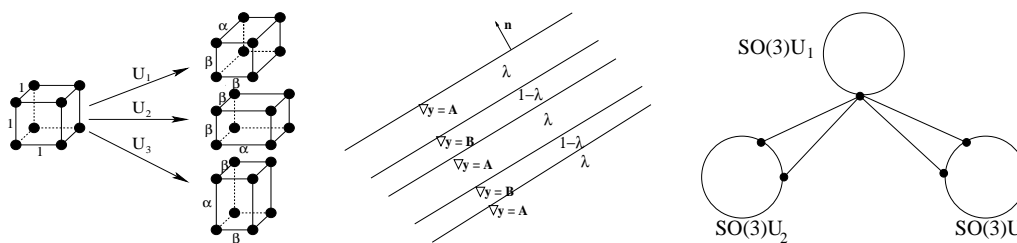


Fig. 2.1. The cubic-to-tetragonal martensitic transformation. Left: The transformation matrices $U_1 = \text{diag} \{\alpha, \beta, \beta\}$, $U_2 = \text{diag} \{\beta, \alpha, \beta\}$, and $U_3 = \text{diag} \{\beta, \beta, \alpha\}$. Middle: a twining deformation composed of two compatible matrices $A = R_i U_i$ and $B = R_j U_j$. Right: Energy wells and rank-one connections.

One of the most commonly observed martensitic microstructures is a fine-scale twinning or simple laminate. It is a periodical structure, with the period of a few atomic distances, consisting of parallel and alternating bands of two coherent variants $R_i U_i$ and $R_j U_j$ with R_i, R_j proper rotations, cf. Fig. 2.1 (middle). Such a microstructure can be described by a continuous deformation y of the austenite that has the gradient ∇y equal to $A = R_i U_i$ and $B = R_j U_j$ alternatively. By the classical Hadamard jump

condition,² the two matrices A and B must be compatible or rank-one connected, i.e., $A - B = a \otimes n$ for some $a \in \mathbb{R}^3$, where n is a unit normal of parallel planes separating the regions A and B .

A martensitic microstructure can be modeled as a deformation that minimizes an energy functional

$$\mathcal{E}(y) = \int_{\Omega} \phi(\nabla y(x)) \, dx \quad (2.1)$$

over a set of deformations $y : \Omega \rightarrow \mathbb{R}^3$ that satisfy certain boundary conditions. Here, $\Omega \subset \mathbb{R}^3$ is the reference configuration, the undeformed austenite of the crystal, and $\phi : \mathbb{R}^{3 \times 3} \rightarrow \mathbb{R}$ a temperature-dependent energy density, where $\mathbb{R}^{3 \times 3}$ denotes the set of all 3×3 real matrices. The energy density ϕ is rotationally invariant, i.e., $\phi(RF) = \phi(F)$ for all $F \in \mathbb{R}^{3 \times 3}$ and all $R \in \text{SO}(3)$, where $\text{SO}(3)$ is the set of all proper rotations. Below the transformation temperature, it is minimized, with the minimum value rescaled to be 0, on multiple energy wells $\text{SO}(3)U_k$ ($k = 1, \dots, N$) that represent martensitic variants (cf. Fig. 2.1, left and right):

$$\phi(F) \geq 0 \quad \forall F \in \mathbb{R}^{3 \times 3} \quad \text{and} \quad \phi(F) = 0 \iff F \in \text{SO}(3)U_1 \cup \dots \cup \text{SO}(3)U_N. \quad (2.2)$$

Often, a matrix A in an energy well is rank-one connected to two matrices B_1, B_2 in a different energy well, and any matrix $\lambda A + (1 - \lambda)B_i$ ($0 < \lambda < 1, i = 1, 2$) is not in any energy wells, cf. Fig. 2.1 (right). The density ϕ is thus not rank-one convex, hence not quasiconvex,³ and the functional (2.1) may not have a minimizer. One then studies, instead, energy-minimizing sequences of deformations, and uses Young measures generated by the corresponding gradient sequences to describe microstructure.

2.1 Uniqueness of a simply laminated martensitic microstructure

How Dirichlet boundary conditions, which model dead loading in an experiment, determine energy-minimizing microstructure is of practical interest. For instance, the simple laminate composed of two rank-one connected variants $A = R_i U_i$ and $B = R_j U_j$ with volume fractions λ and $1 - \lambda$ (cf. Fig. 2.1, middle) is an energy-minimizing microstructure with respect to the boundary condition

$$y(x) = F_{\lambda} x \quad \forall x \in \partial\Omega, \quad \text{where} \quad F_{\lambda} = \lambda A + (1 - \lambda)B. \quad (2.3)$$

This means that there exists an energy-minimizing sequence of Lipschitz-continuous deformations $y_k : \Omega \rightarrow \mathbb{R}^3$ satisfying the boundary condition (2.3), such that the corresponding sequence of gradients ∇y_k generates the homogeneous Young measures

$$\nu_x = \lambda \delta_A + (1 - \lambda) \delta_B \quad \text{a.e. } x \in \Omega, \quad (2.4)$$

where δ_G denotes the Dirac measure at G . Such deformations y_k can be explicitly constructed (cf. Chipot and Kinderlehrer, Arch. Rational Mech. Anal., 103, 237–277, 1988).

Is such a simply laminated microstructure uniquely determined by the boundary condition (2.3)? The answer is not obvious when a martensitic crystal has more than two variants ($N > 2$), since the mixture of other variants can possibly accommodate the boundary condition (2.3), which is in fact true for certain lattice parameters, cf. [9]. Ball and James (Phil. Trans. R. Soc. Lond. A, 338, 389–450, 1992) proved such uniqueness for the cases $N = 2$ and $N = 3$, but left the general case open. In [9],

²Given $A, B \in \mathbb{R}^{3 \times 3}$ and $n \in \mathbb{R}^3$ with $n \neq 0$. There exists a continuous mapping $y : \mathbb{R}^3 \rightarrow \mathbb{R}^3$ such that $\nabla y = A$ and $\nabla y = B$ respectively, on the two sides of a given plane with normal n , if and only if $A - B = a \otimes n$ for some $a \in \mathbb{R}^3$.

³A continuous function $\phi : \mathbb{R}^{3 \times 3} \rightarrow \mathbb{R}$ is quasiconvex, if $\phi(F) \leq \int_{(0,1)^3} \phi(F + \nabla v) \, dx$ for all $F \in \mathbb{R}^{3 \times 3}$ and all $v \in C_c^\infty((0,1)^3, \mathbb{R}^3)$. Under mild assumptions, the quasiconvexity of the density ϕ is equivalent to the sequential weak lower semicontinuity, which implies the existence of a minimizer, of the functional (2.1). In general, polyconvexity (convex in subdeterminants) \implies quasiconvexity \implies rank-one convexity (convex in any line connecting two rank-one connected matrices) \implies convexity. See, e.g., C. B. Morrey Jr., Multiple Integrals in the Calculus of Variations, Springer, 1966, and B. Dacorogna, Direct Methods in the Calculus of Variations, Springer, 2007.

Bahttacharya, Luskin, and I proved such uniqueness for $N = 6$. Our methods are general and have been applied to the cases $N = 4$ (Belik and Luskin, *Math. Model. Numer. Anal.*, 34, 663–685, 2002) and $N = 12$ (Efendiev and Luskin, *Math. Comp. Model.*, 34, 1289–1305, 2002).

The key in our proof was to reduce a general N -well problem to a two-well one by proving the volume fraction of k th variant $\tau_k := \int_{\Omega} \nu_x(\text{SO}(3)U_k) dx = 0$ if $k \neq i, j$, where U_i and U_j are the variants in the boundary data F_{λ} . Such reduction can be made by choosing suitable vectors $w \in \mathbb{R}^3$ in

$$\begin{aligned} \sum_{k \neq i, j} \tau_k (|U_k w|^2 - |F_{\lambda} w|^2) &= \int_{\Omega} \int_{\mathbb{R}^{3 \times 3}} |(G - F_{\lambda}) w|^2 d\nu_x(G) dx \geq 0 \quad \text{if } w \cdot n = 0, \\ \sum_{k \neq i, j} \tau_k \left[|(\text{Cof } U_k) w|^2 - |(\text{Cof } F_{\lambda}) w|^2 \right] &= \int_{\Omega} \int_{\mathbb{R}^{3 \times 3}} |(\text{Cof } G - \text{Cof } F_{\lambda}) w|^2 d\nu_x(G) dx \geq 0 \quad \text{if } w \cdot A^{-1} a = 0, \end{aligned}$$

These inequalities follow from the minors relations, and the rank-one connections $A - B = a \otimes n$ and $\text{Cof } A - \text{Cof } B = -(\det A)B^{-T}n \otimes A^{-1}a$.

2.2 A stability theory and numerical analysis of martensitic microstructure

The numerical analysis of nonconvex variational problems modeling microstructure is in general quite unconventional. Early work along this line dealt only with nonphysical scalar problems. Luskin (*Numer. Math.*, 75, 205–221, 1996) gave the first and systematic analysis of finite-element approximations of the unique simply laminated microstructure that “minimizes” the functional (2.1) with $N = 2$ subject to the boundary condition (2.3). In this analysis, a series of stability estimates for all the admissible deformations $y : \Omega \rightarrow \mathbb{R}^3$ are first obtained. These include the estimate for the strong convergence of deformations and that of deformation gradients tangential to twin planes

$$\int_{\Omega} |y(x) - F_{\lambda} x|^2 dx + \int_{\Omega} |[\nabla y(x) - F_{\lambda}] w|^2 dx \leq C \mathcal{E}(y)^{1/2} \quad \forall w \in \mathbb{R}^3 \text{ with } w \cdot n = 0,$$

where $C > 0$ is a generic constant independent of y , weak convergence of deformation gradients, approximations of volume fractions, and particularly approximations of Young measures (2.4) given by

$$\left| \int_{\Omega} \{f(x, \nabla y(x)) - [\lambda f(x, A) + (1 - \lambda)f(x, B)]\} dx \right| \leq C(f) \mathcal{E}(y)^{1/4} \quad \forall \text{ smooth } f : \Omega \times \mathbb{R}^{3 \times 3} \rightarrow \mathbb{R}.$$

The energy estimate $\min_{z_h \in \mathcal{A}_h} \mathcal{E}(z_h) \leq Ch^{1/2}$ is also obtained by construction, where \mathcal{A}_h is the set of all admissible finite-element deformations. The error estimates for any finite-element energy minimizer y_h are then derived by replacing y by y_h in the stability estimates.

In a series of papers [4–6], Luskin and I extended this analysis to the simply laminated microstructure governed by a three-well energy density and with varying volume fractions, and to a class of nonconforming finite-element approximations of such a microstructure. In [9], Bhattacharya, Luskin, and I derived stability estimates for a six-well energy density. In particular, we obtained the reduction estimate $\tau_k(y) \leq C \mathcal{E}(y)^{1/2}$ for the volume fraction of the k th variant that is not in the microstructure.

In [10, 12], I studied a large class of martensitic microstructures that are not necessarily uniquely determined by the boundary data. I obtained the uniqueness of macroscopic deformations of microstructures and some of the stability estimates. For a boundary data that determines a laminate of order $q \geq 2$, I constructed finite-element approximations y_h to obtain the energy estimate $\mathcal{E}(y_h) \leq Ch^{1/(q+1)}$, cf. Fig. 2.2, and the related error estimates. Finally, I proved that the projection $\pi : \mathbb{R}^{3 \times 3} \rightarrow \cup_{k=1}^N \text{SO}(3)U_k$, defined by

$$\|\pi(F) - F\| = \min \{ \|G - F\| : G \in \cup_{k=1}^N \text{SO}(3)U_k \} \quad \forall F \in \mathbb{R}^{3 \times 3},$$

is Lebesgue-measurable and continuous except on a closed subset of $\mathbb{R}^{3 \times 3}$ of measure zero. This projection has been a key tool in all the previously mentioned analysis.

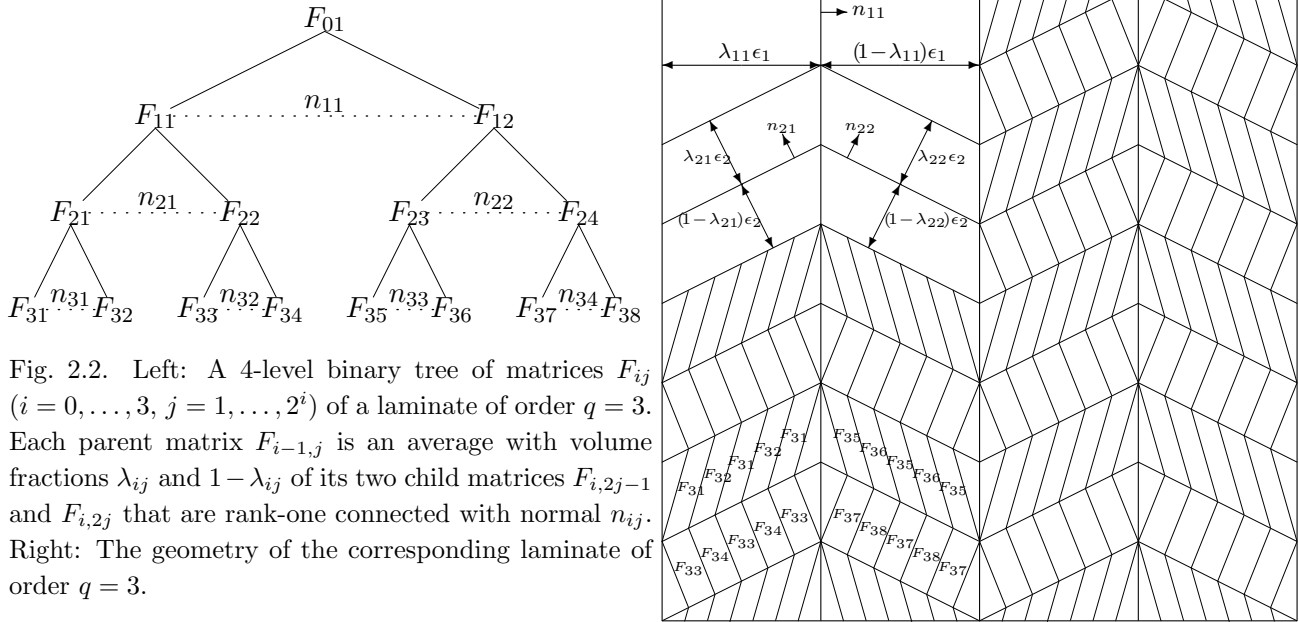


Fig. 2.2. Left: A 4-level binary tree of matrices F_{ij} ($i = 0, \dots, 3, j = 1, \dots, 2^i$) of a laminate of order $q = 3$. Each parent matrix $F_{i-1,j}$ is an average with volume fractions λ_{ij} and $1 - \lambda_{ij}$ of its two child matrices $F_{i,2j-1}$ and $F_{i,2j}$ that are rank-one connected with normal n_{ij} . Right: The geometry of the corresponding laminate of order $q = 3$.

2.3 Numerical modeling of the Chu–James needle-like microstructure

In their biaxial loading experiment on a shape-memory alloy Cu–Al–Ni single crystal, Chu and James discovered a needle-like microstructure in which layers of one variant of the crystal form long, bent, and branched needles ending at a flat interface while layers of another variant are compatible with a homogeneous state at the interface, cf. Fig. 2.3, left (courtesy of R. D. James). Physical properties of this microstructure could not be easily explained by a purely analytical approach.

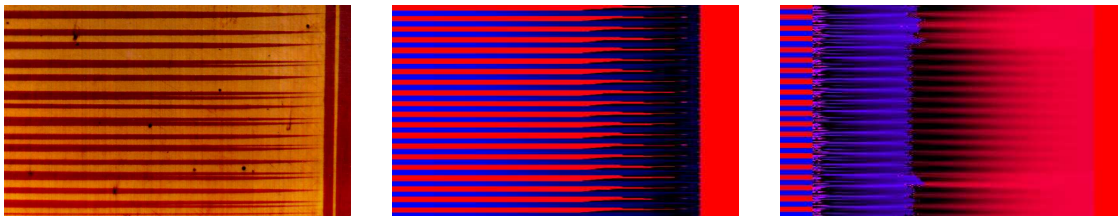


Fig. 2.3. Left and middle: The Chu–James needle-like microstructure: experiment (left) and computer simulation (middle). Right: A computer simulated microstructure of multiple layers with different length scales.

In my Ph.D. thesis (University of Minnesota, 1996) under the direction of Luskin and my work [7] with Luskin, we developed a geometrically nonlinear model and finite-element optimization code for computing the microstructure.⁴ Our analysis using such a model predicted the orientation misfit agreeing well with the experiment. Fig. 2.3 (middle) shows our computer simulated needle-like microstructure with bent and branched needles. Fig. 2.3 (right) shows a microstructure discovered by our numerical computation that was in fact experimentally observed earlier (Flippen and Haas, *Solid State Commun.*, 13, 1207–1209, 1973; Meeks and Auld, *Appl. Phys. Lett.*, 47, 102–104, 1985).

3 Epitaxial Growth of Thin Films

Epitaxial growth is a widely used technique to grow thin solid films by depositing atoms or molecules onto an existing layer of material. It has important applications in nanotechnologies. Microscopic processes in epitaxial growth include the deposition of atoms from the gas phase onto a film surface,

⁴This model was suggested to us by Robert Kohn. The energy density used in the computation was constructed by Richard James to match material parameters.

desorption of adatoms (adsorbed atoms) from such surface into the gas phase, surface diffusion of adatoms, attachment and detachment of adatoms to and from atomic steps or island boundaries, nucleation of adatom islands, and island coalescence, cf. Fig. 3.1. These processes are often far from equilibrium and span several decades of spatial and temporal scales. They determine the quality of growing thin films.

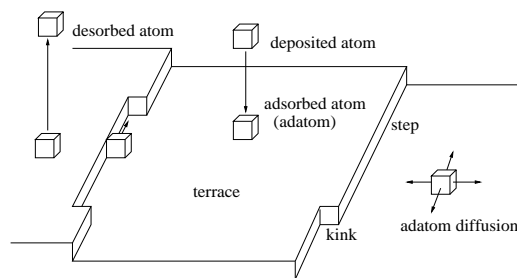


Fig. 3.1. Epitaxial growth of thin films.

3.1 Analysis and improvement of island dynamics models

Burton, Cabrera, and Frank (Phil. Trans. Roy. Soc. Lond. Ser. A, 243, 299–358, 1951) developed a moving-boundary model for step-flow growth of thin films: the adatom density solves a diffusion equation on terraces with an equilibrium boundary condition and step edges move with a velocity determined from the two-sided diffusive flux to the boundary, cf. Fig. 3.2. This BCF model has been widely used for many decades. However, its assumption on equilibrium steps is invalid in many experimental situations in which the growth of thin films is far from equilibrium. To include the missing kinetics, Cafilisch *et al.* (Phys. Rev. E, 59, 6879–6887, 1999) developed a kinetic step-edge model for moving step edges with velocity determined by the adatom density, edge-adatom density, and kink convection equations, respectively. This kinetic description is more accurate but also more complicated than the BCF model.

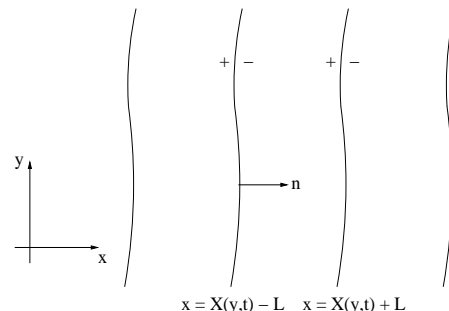


Fig. 3.2. Step-flow growth. The symbol + (-) indicates an upper (lower) terrace.

Aiming at developing a BCF-type model that could include the kinetics via the boundary conditions for adatom diffusion, in [11], Cafilisch and I first analyzed the stability of moving, straight step edges within the kinetic description. We then applied an asymptotic analysis to derive a new set of boundary

conditions for the adatom terrace diffusion, which is a kinetic version of the Gibbs–Thomson relation,

$$\begin{aligned} -D_T \nabla \rho_+ \cdot \mathbf{n} &= D_T (\rho_+ - \rho_*) - \mu \kappa, \\ D_T \nabla \rho_- \cdot \mathbf{n} &= D_T (\rho_- - \rho_*) - \mu \kappa, \end{aligned}$$

and the normal velocity v_n that includes the “surface diffusion” κ_{yy} along step edges

$$v_n = D_T (\rho_+ + \rho_-) - 2D_E \phi + \beta \rho_{*yy} + \nu \kappa_{yy}.$$

Here, ρ_{\pm} are adatom densities on upper/lower terraces, ϕ the edge-adatom density, D_T , D_E the corresponding diffusion constants, ρ_* a reference adatom density, κ the curvature, and μ , ν , and β constants. To the best of our knowledge, this derivation is the first that is based on kinetics rather than thermodynamics.

With the new set of boundary conditions and velocity law, Rätz, Voigt, and I studied the morphological stability of a single, circular, epitaxially growing adatom island [17]. We found that the Bales–Zangwill instability (Phys. Rev. B, 41, 5500–5508, 1990) for a straight step edge disappears for a circular island. This was confirmed by our numerical simulation reported in [16], cf. Fig. 3.3.

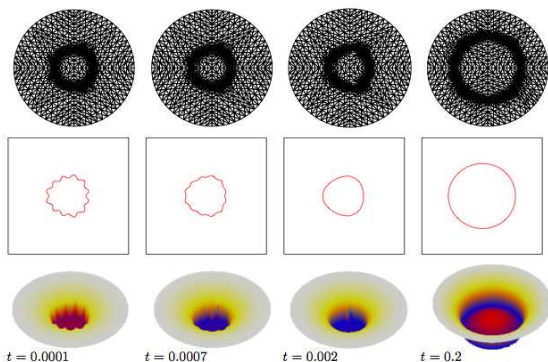


Fig. 3.3. Meshes, boundaries, and densities.

3.2 An adaptive finite-element method for island dynamics

In [16], my collaborators and I developed an adaptive finite-element method for the numerical simulation of island dynamics. We used a variational treatment of the one-dimensional “surface diffusion”, avoiding

complicated discretization of fourth-order partial derivatives on a curves as commonly done in a finite-difference level-set method. Our extensive numerical tests, including the one on a growing circular island (cf. Fig. 3.3), demonstrate that our method is stable, efficient, and accurate.

3.3 Instabilities, coarsening, and dynamic scaling: Analysis of continuum models

In epitaxial growth of thin films, morphological instabilities occur as the film thickness reaches a critical value. Such instabilities manifest themselves as a sort of spinodal decomposition, triggering the nucleation of atomic islands. The nuclei then evolve into mounds, and the mound structure coarsens as the number of mounds decreases. Experiments and numerical simulations suggest that the well-characterized lateral size of mounds, $\lambda(t)$, increases as $\lambda(t) \propto t^n$, where t is time and $n > 0$ a constant called the coarsening exponent. The interface width $w(t)$, which is the standard deviation of height, also increases as $w(t) \propto t^\beta$ for some constant $\beta > 0$ called the growth exponent, cf. Fig. 3.4. When the finite size of the system becomes effective, the interface width saturates with the saturated value $w_s(L) \propto L^\alpha$, where L is the linear size of the system and $\alpha > 0$ a constant called the roughness exponent. The saturation time satisfies the dynamic scaling law $t_s(L) \propto L^{\alpha/\beta}$.

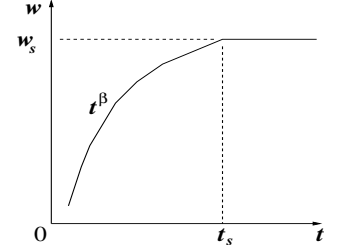


Fig. 3.4. Scaling.

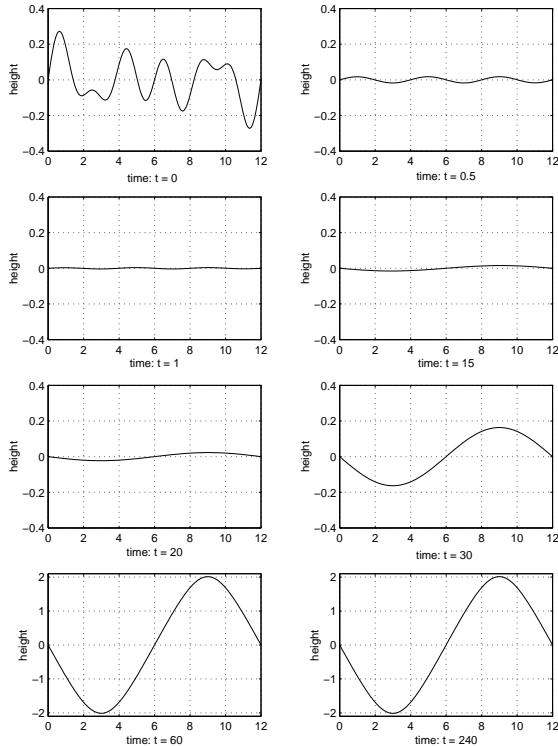


Fig. 3.5. Nonlinear morphological instability.

Schwoebel effect: in order to stick to a step edge from an upper than a lower terrace, adatoms must overcome a higher energy barrier. This model predicts that the slope of mounds grows unboundedly with respect to the system size, and is thus called a no-slope-selection model.

In [14], Liu and I proved the well-posedness of these models. We also demonstrated by weakly nonlinear analysis and numerical simulation a morphological instability in the rough-smooth-rough pattern: the initially linearly stable modes are damped quickly but their interactions generate slowly a new and linearly unstable mode, cf. Fig. 3.5. Our findings agree with the experiment reported by Gyure *et al.* (Phys. Rev. Lett., 81, 4931–4934, 1998).

Heuristic arguments predict the coarsening and growth exponents $n = \beta = 1/3$ for the slope-selection dynamics. Kohn and Yan (Commun. Pure Appl. Math., 56, 1549–1564, 2003) obtained

For years, considerable efforts have been made in the physics community in developing continuum models to study scaling laws which characterize mechanisms of epitaxial growth. Such a model is a partial differential equation $\partial_t h = -\nabla \cdot \mathbf{j}$ of the macroscopic height profile $h = h(x, t)$ in a co-moving frame, where $x = (x_1, x_2)$, together with a given surface flux $\mathbf{j} = \mathbf{j}(\nabla h, \nabla^2 h, \dots)$. Two commonly used such equations are

$$\partial_t h = -\Delta^2 h + \nabla \cdot [(1 - |\nabla h|^2) \nabla h], \quad (3.1)$$

$$\partial_t h = -\Delta^2 h + \nabla \cdot \left(\frac{\nabla h}{1 + |\nabla h|^2} \right). \quad (3.2)$$

They are gradient flows of the effective energy functionals

$$E_1(h) = \int_{(0,L)^2} \left[\frac{1}{2} |\Delta h|^2 + \frac{1}{4} (|\nabla h|^2 - 1)^2 \right] dx, \quad (3.3)$$

$$E_2(h) = \int_{(0,L)^2} \left[\frac{1}{2} |\Delta h|^2 - \frac{1}{2} \log(1 + |\nabla h|^2) \right] dx, \quad (3.4)$$

respectively. The first one predicts a fixed slope (scaled to be 1) of mounds, and is thus called the slope-selection model. The second one models particularly the Ehrlich–

rigorously an upper bound for the averaged coarsening rate. Their argument, however, does not seem to apply directly to the no-slope-selection dynamics which predicts the unusual coarsening exponent 1/4 and growth exponent 1/2.

In [18], Liu and I studied systematically the no-slope-selection model. We obtained two classes of results. First, by using the energy method and convexity arguments, we obtained a series of bounds for the pointwise interface width, averaged slope, and averaged energy

$$w(t) \leq O(t^{1/2}), \quad \left(\int_{t_0}^t \int_{(0,L)^2} |\nabla h(x, \tau)|^2 dx d\tau \right)^{1/2} \leq O(t^{1/4}), \quad \text{and} \quad \int_{t_0}^t E_2(h(\tau)) d\tau \geq O(-\log t),$$

respectively. We also obtained bounds for the saturated interface width and saturation time in the dynamic scaling. All of these results confirm the earlier predictions based on heuristic arguments.

Second, by studying the singularly perturbed functionals derived from (3.4) with the scaling $L \rightarrow \varepsilon = 1/L$ and $h(x) \rightarrow \varepsilon h(x/\varepsilon)$, we obtained the large-system asymptotics

$$\min_h E_2(h) \sim -\log L \quad \text{and} \quad \sqrt{\int_{(0,L)^2} |\nabla^m h_{min}|^2 dx} = O(L^{2-m}) \quad (m = 0, 1, 2) \quad \text{as } L \rightarrow \infty,$$

where h_{min} is a $(0, L)^2$ -periodical minimizer of E_2 . These and a scaling argument enabled us to construct a sequence of $(0, L/j)^2$ -periodical equilibria with decreasing energies. Our analysis indicated that an underlying system evolves in such a way that it always stays close to such periodic equilibria.

In my work [19, 20], I further proved that, in the large-system limit, the functional (3.4) Γ -converges to the Villain functional (J. de Phys. I, 1, 19–42, 1991), which is similar to (3.4) with the logarithm term replaced by $\log |\nabla h|$. I also generalized the analysis to no-slope-selection models with high-order surface diffusion terms.

4 Variational Implicit-Solvent Modeling and Simulation of Biomolecular Interactions

Implicit or continuum solvent models are widely used for efficient calculations of solvation free energies and biomolecular structures which determine crucially biomolecular processes and functions such as protein folding and molecular recognition. In such a model, the solvent molecules and ions are treated implicitly and their effects are coarse-grained. Most of the existing implicit-solvent models begin with the generation of a solute-solvent interface. Such an interface is then used to calculate the surface energy, proportional to the surface area, and as the dielectric boundary to calculate the electrostatic free energy by the Poisson–Boltzmann or generalized Born model. The total solvation free energy is finally obtained as the sum of these nonpolar and polar contributions.

Recently, Dzubiella, Swanson, and McCammon (Phys. Rev. Lett., 96, 087802, 2006; J. Chem. Phys., 124, 084905, 2006) proposed a variational implicit-solvent model (VISM). In this formulation, the solvation free energy and stable solute-solvent interfaces are obtained by minimizing a solvation free-energy functional of all possible surfaces Γ that surround all the fixed solute atoms x_1, \dots, x_N (cf. Fig. 4.1):

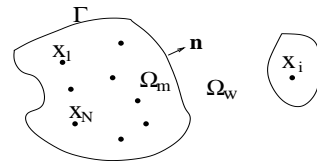


Fig. 4.1. The VISM geometry.

$$G[\Gamma] = \underbrace{P \text{Vol}(\Omega_m) + \gamma_0 \int_{\Gamma} (1 - 2\tau H) dS}_{G_{geo}[\Gamma]: \text{geometrical contributions}} + \underbrace{\rho_0 \sum_{i=1}^N \int_{\Omega_w} U_{LJ}^{(i)}(|x - x_i|) dV(x)}_{G_{vdW}[\Gamma]: \text{van der Waals interactions}} + G_{elec}[\Gamma]. \quad (4.1)$$

Here, Ω_m and Ω_w are the solute (molecule) and solvent (water) regions, respectively, separated by the interface Γ , P the pressure difference, γ_0 the surface tension of a flat interface, τ , often called the

Tolman length, a parameter of correction to surface tension, H the mean curvature, ρ_0 the bulk solvent density, and $U_{LJ}^{(i)}$ is the Lennard-Jones potential for the i th solute atom.

The H term in the geometrical part $G_{geo}[\Gamma]$ is the correction to the surface tension which is no longer a constant for nanoscaled systems. The form of this correction is a generalization of that for a spherical solute in the classical scaled-particle theory. The terms in $G_{geo}[\Gamma]$ are the same as those predicted in Hadwiger’s Theorem,⁵ except that the integral of Gaussian curvature K is neglected, since it is a constant when no topological changes are involved. The last term $G_{elec}[\Gamma]$ is the electrostatic energy which will be discussed more in Subsection 4.2 below.

A significant part of my recent research is on the solvation of biomolecules, jointly with the group of biochemists who developed the new solvation model, and other mathematicians, see [21, 23, 25, 28–30] in which, except [30], I am the corresponding author. I myself have also studied the Poisson–Boltzmann theory for continuum electrostatics [26, 27]. All of these are described in more details below. Currently, we are working on fast numerical methods for electrostatics, the Langevin dynamics for solute-solvent interface, and a multiscale variational approach. I myself am looking further into the scaled-particle theory, statistical mechanics basis of the Poisson–Boltzmann theory, and Poisson–Nernst–Planck systems.

4.1 Coupling molecular mechanics of solute with implicit-solvent: a level-set variational approach

In [21, 28, 29], my collaborators and I developed a level-set method to minimize the free-energy functional (4.1) for non-polar molecular systems (i.e., $G_{elec}[\Gamma] = 0$).

The starting point of a level-set method is to represent a surface Γ by the zero level-set of a function $\phi : \mathbb{R}^3 \rightarrow \mathbb{R}$, called a level-set function, i.e., $\Gamma = \{x \in \mathbb{R}^3 : \phi(x) = 0\}$. For a surface $\Gamma(t)$ that moves with normal velocity $v_n = v_n(x(t)) = \dot{x}(t)$ ($x(t) \in \Gamma(t)$), the level-set function $\phi = \phi(x, t)$ is determined by the level-set equation $\partial_t \phi + v_n |\nabla \phi| = 0$ on $\Gamma(t)$. This normal velocity is extended away from the moving surface $\Gamma(t)$ so that the level-set equation can be solved on a computational box.

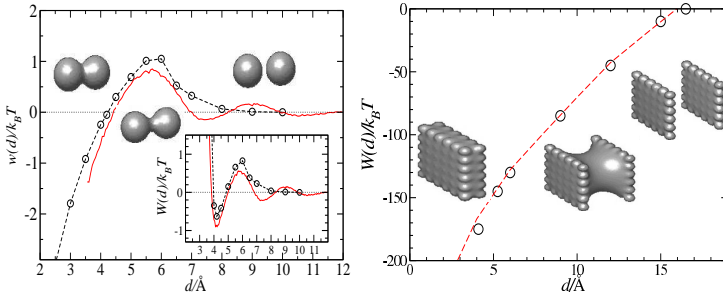


Fig. 4.2. Comparison of the level-set VISM (circles) with MD (solid lines) simulations for two xenon particles and two plates.

We invented a series of techniques, such as the precomputation of the potential, numerical regularization, and fast numerical integration, for the level-set simulations of this geometrical motion.

Our extensive numerical tests have shown that our level-set VISM is very accurate compared with molecular dynamics (MD) simulations, cf. Fig. 4.2. It captures the hydrophobic (or dewetting) properties, cf. Fig. 4.2 (right) and Fig. 4.3 (left), and reproduces the bimodal (bistable) property, cf. Fig. 4.3 (right) for the two branches of the potential of mean force (PMF). Our approach is also efficient for simulating large biomolecules, cf. Fig. 4.4.

⁵**Hadwiger’s Theorem.** Let C denotes the set of all convex compact subsets of \mathbb{R}^3 and M the set of all finite unions of members of C . Let $F : M \rightarrow \mathbb{R}$ be a translationally and rotationally invariant mapping. Suppose $F(U \cup V) = F(U) + F(V) - F(U \cap V)$ for all $U, V \in M$ and $F(U_k) \rightarrow F(U)$ if $U_k \in C$ ($k = 1, 2, \dots$), $U \in C$, and $U_k \rightarrow U$ with respect to the Hausdorff distance of sets. Then there exist $a_i \in \mathbb{R}$ ($i = 1, \dots, 4$) such that $F(U) = a_1 \text{Vol}(U) + a_2 \text{Area}(\partial U) + a_3 \int_{\partial U} H dS + a_4 \int_{\partial U} K dS$ for all $U \in M$.

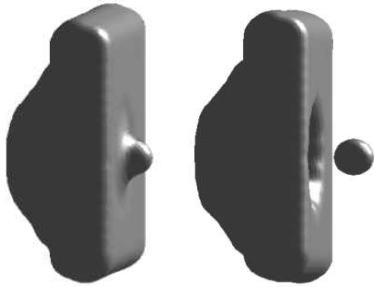


Fig. 4.3. Dewetting (left), drying (middle), and bimodal PMF (right) of a receptor-ligand system simulated by the level-set VISM.

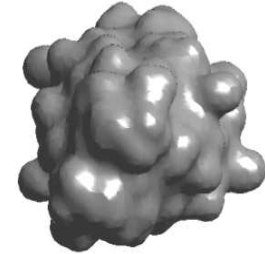
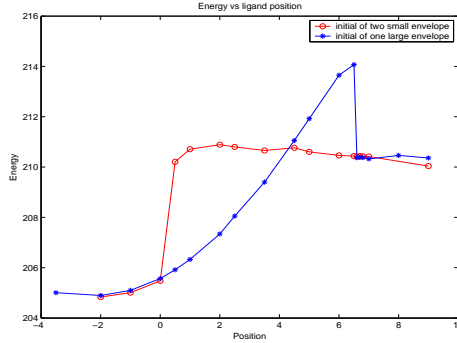


Fig. 4.4. A large molecule.

The work [25] presents a new and hybrid approach that couples the level-set VISM with the molecular mechanics of solutes whose atoms are now degrees of freedom. We propose an effective Hamiltonian

$$H[x_1, \dots, x_N; \Gamma] = M[x_1, \dots, x_N] + G[x_1, \dots, x_N; \Gamma],$$

in which the M term is the molecular force field of solute atoms that includes the usual terms of van der Waals dispersion, bonding, bending, and torsion, and the G term is the same as (4.1). This Hamiltonian determines the following equations for the relaxation of solute particles $x_i = x_i(t)$ ($1 \leq i \leq N$) and solute-solvent interface $\Gamma(t)$:

$$\dot{x} = -M_i \nabla_{x_i} H \quad (i = 1, \dots, N) \quad \text{and} \quad v_n = -M \delta_\Gamma H[\Gamma] = -M \delta_\Gamma G[\Gamma],$$

where M_i and M are suitable mobilities and the normal velocity v_n is given by (4.2). These equations are solved iteratively. Our numerical results show the motion of particles and that of the interface influence each other, cf. Fig. 4.5 and Fig. 4.6. This is clearly the first step toward accurate and efficient modeling with implicit solvent of conformational changes of biomolecules.

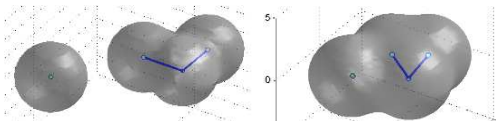


Fig. 4.5. The relaxation of a four-atom model system.

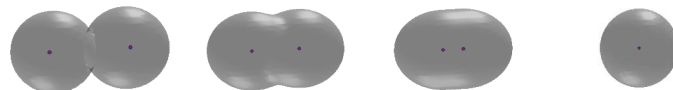


Fig. 4.6. The relaxation of two non-interacting particles, showing that the motion of interface controls that of particles.

4.2 Effective electrostatic surface forces

The electrostatic free energy $G_{elec}[\Gamma]$ in (4.1) is usually determined by the Poisson–Boltzmann (PB) or generalized Born model. Consider the Poisson equation $-\nabla \cdot \varepsilon \nabla \psi = 4\pi \rho$ for the electrostatic potential ψ . In an implicit-solvent description, the dielectric coefficient $\varepsilon = \varepsilon_\Gamma$ is piecewise constant in the solute and solvent regions, respectively. The charge density is $\rho = \rho_f + \chi_w \sum_{i=1}^M q_i c_i$, where the fixed part ρ_f consists of point charges of solute atoms, χ_w is the characteristic function of the solvent region Ω_w , and c_i 's are the concentrations of ionic species (M of them assumed) in the solvent with charge q_i 's. Assuming the Boltzmann distribution $c_i = c_i^\infty e^{-\beta q_i \psi}$ for equilibrium ionic concentrations c_i , where β is the inverse thermal energy and c_i^∞ the bulk concentration, one then obtains the PB equation (PBE)

$$-\nabla \cdot \varepsilon_\Gamma \nabla \psi - 4\pi \chi_w \sum_{i=1}^M q_i c_i^\infty e^{-\beta q_i \psi} = 4\pi \rho_f. \quad (4.3)$$

The corresponding electrostatic free energy is then given by

$$G_{elec}[\Gamma] = \int \left[-\frac{\varepsilon(x)}{8\pi} |\nabla\psi|^2 + \rho_f(x)\psi - \beta^{-1}\chi_w \sum_{i=1}^M c_i^\infty \left(e^{-\beta q_i \psi} - 1 \right) \right] dx. \quad (4.4)$$

In [23], my collaborators and I first pointed out that this commonly used functional (4.4) of electrostatic free energy is not convex in ψ , and therefore does not lead to the correct variational principle. We then proposed an electrostatic free-energy functional of ionic concentrations $c = (c_1, \dots, c_M)$ ⁶

$$F[c] = \int \left[\frac{1}{2} \left(\rho_f + \chi_w \sum_{i=1}^M q_i c_i \right) \psi + \beta^{-1} \chi_w \sum_{i=1}^M c_i \log c_i + \text{terms linear in } c \right] dV, \quad (4.5)$$

where ψ is determined by the Poisson equation with $\rho = \rho_f + \chi_w \sum_{i=1}^M q_i c_i$, and derived from the convex functional (4.5) the Boltzmann distributions for equilibrium concentrations c_1, \dots, c_M and potential ψ , leading to the PBE (4.3).

We further derived rigorously the variational derivative

$$\delta_\Gamma G_{elec}[\Gamma](x) = \frac{1}{8\pi} \left(\frac{1}{\varepsilon_m} - \frac{1}{\varepsilon_w} \right) |\varepsilon_\Gamma(x) \nabla\psi(x)|^2 + \sum_{j=1}^M \beta^{-1} c_j^\infty \left[e^{-\beta q_j \psi(x)} - 1 \right] \quad \forall x \in \Gamma, \quad (4.6)$$

where ε_m and ε_w are the dielectric constants in the solute and solvent regions Ω_m and Ω_w , respectively. The distribution $-\delta_\Gamma G_{elec}[e\Gamma]$ is the normal component of the effective electrostatic surface force. It is the polar component of the normal velocity v_n (cf. (4.2)) in our level-set relaxation.

Using (4.6), the charge neutrality, and Jensen's inequality, we proved that this force is always attractive to biomolecules, confirming rigorously within the framework of implicit solvent a known theory (cf. B. Chu, *Molecular Forces, Based on the Lecture of Peter J. W. Debye*, Wiley, 1967).

5 Analysis, Improvement, and Application of the Poisson–Boltzmann Theory of Continuum Electrostatics

5.1 Variational properties and excluded-volume effects

In [26], I gave a rigorous mathematical analysis of the PBE (4.3) and the related free-energy functional (4.5). Specifically, I obtained the following main results:

- (1) The functional (4.5) has a unique minimizer. This is proved by direct methods in the calculus of variations, using the fact that the functional (4.5) is convex and the entropic terms $c_i \log c_i$ are superlinear. The singularities due to the point charges of solute atoms in the fixed part ρ_f of charge density are removed by using the full-space Green's functions;
- (2) The unique minimizer of (4.5) has uniform and pointwise upper and lower bounds. This follows from Lemma 5.1 below;
- (3) The boundary-value problem of the PBE (4.3) has a unique solution which is related to the unique free-energy minimizing concentrations by the Boltzmann distributions;
- (4) The boundary-value problem of PBE is equivalent to its interface formulation which is often used in boundary-integral numerical calculations.

All of these rely on the following lemma that can be proved by delicate and technical constructions, using the fact that the function $s \mapsto s \log s$ has a large derivative in magnitude for s near 0 or ∞ :

Lemma 5.1. *For any set of concentrations $c = (c_1, \dots, c_M)$, there exists a set of concentrations $\bar{c} = (\bar{c}_1, \dots, \bar{c}_M)$ such that: (1) \bar{c} is close to c ; (2) There are two positive constants θ_1 and θ_2 such that $\theta_1 \leq \bar{c}_i(x) \leq \theta_2$ a. e. x for all $i = 1, \dots, M$; and (3) $F[\bar{c}] \leq F[c]$.*

⁶Variants of such a functional existed before in the literature.

It is well known that the classical PB model does not account for the excluded-volume effect and can hence lead to large equilibrium ionic concentrations. Attempting to generalize the PB model to include such effects, in [27], I proposed and studied the following free-energy functional of the ionic concentrations c_1, \dots, c_M in an ionic solution occupying a bounded region $\Omega \subset \mathbb{R}^3$:

$$\hat{F}[c] = \int_{\Omega} \left\{ \frac{1}{2} \rho \psi + \beta^{-1} \sum_{i=0}^M c_i [\log(a_i^3 c_i) - 1] + \text{terms linear in } c \right\} dx. \quad (5.7)$$

Here, $\rho = \sum_{i=1}^M q_i c_i$ is the charge density, ψ the electrostatic potential determined by the Poisson equation together with some boundary conditions, $\varepsilon : \Omega \rightarrow \mathbb{R}$ a variable dielectric coefficient, a_i for $1 \leq i \leq M$ the linear size of ions of i th species, a_0 of solvent molecules, and c_0 the solvent concentration defined by $\sum_{i \geq 0} a_i^3 c_i = 1$. Note that the summation in the β^{-1} term starts from $i = 0$,

The functional (5.7) is in fact convex, and admits a unique minimizer. With a much refined construction, I obtained the result parallel to Lemma 5.1 for \hat{F} with $0 < \theta_1 < \theta_2 < 1$, which shows that in any region there are always some fractions of ions of each species and the solvent molecules. This is in fact contrary to experiments at the molecular level—a drawback of a PB-like mean-field theory, since ions of same type can cluster in a small region of the ionic solution.

If $a_0 = a_1 = \dots = a_M =: a$, then the Euler–Lagrange equations for the equilibrium concentrations c_1, \dots, c_M are given by [27]

$$c_i(x) = \frac{c_i^{\infty} e^{-\beta q_i \psi}}{1 + a^3 \sum_{j=1}^M c_j^{\infty} e^{-\beta q_j \psi}}, \quad i = 1, \dots, M.$$

These are generalized Boltzmann distributions. Otherwise, an explicit form of the dependence of the equilibrium concentrations on the potential seemed unavailable, as had been noticed before in the literature. Nevertheless, I was able to prove the monotonicity of the charge density $\sum_{i=1}^M q_i c_i$ as a function of the potential ψ . This monotonicity implies a variational principle with a convex functional for a generalized, implicit PBE that includes the excluded-volume effect.

My article [27] was selected by the journal editors for inclusion in the IOP (Institute of Physics) Select, which comprises articles “for their novelty, significance and potential impact on future research”, and “reflects both the breadth and international significance of papers published” in the IOP journals.

5.2 Numerical solution of a reduced Poisson–Nernst–Planck system

In [29], my collaborators and I studied a reduced Poisson–Nernst–Planck system for a charged spherical solute immersed in a solvent with multiple diffusive ionic or molecular species that are electrostatically neutralized in the far field. Some of these species are in equilibrium while others are reactive when in contact with the charged solute. We obtained semi-analytical and numerical solutions of the underlying system, calculated the reaction rate for the reactive species, and give a rigorous analysis on the convergence of our numerical algorithm. We compared the results for a reactive system and those for a non-reactive system, and found that two cases were significantly different for certain parameters. For instance, the electrostatic potential for a reactive system can be non-monotone. Our approach provides a means of solving a PNP system which in general does not have a closed-form solution even with a special geometrical symmetry.

6 Numerical methods and analysis of interface motion

Over the years, my research on materials, biochemical, and biophysical problems has led me naturally to study interface motion. My publications [11, 13, 16, 17, 21–26, 28] are all related to such studies. Briefly, I have made the following contributions:

- (1) With my collaborators, I have analyzed stability of moving interfaces with application to epitaxial growth of thin films and to geometrical modeling of molecular surfaces, cf. [11, 17, 21]. I have also introduced new techniques to calculate the first variation of interface-dependent functionals with respect to the location change of the interface, cf. [23];
- (2) I have done numerical analysis for general elliptic interface problems. In [22], my co-authors and I gave a reformulation of such problems with inhomogeneous jump conditions into the one with homogeneous jump conditions, using a single level-set function of the interface. We also gave error estimates for the finite-element immersed-interface method coupled with our new formulation. In [26], I proved the equivalence of the boundary-value problem of PBE and its interface formulation which is often used in the boundary integral numerical calculations of PBE;
- (3) Together with my collaborators, I have developed many new methods and techniques for moving interface problems, such as finite-element immersed interface methods [13, 22], adaptive finite-element front-tracking methods [16, 24], and numerical regularization and fast numerical integration in the level-set method for geometrically based interface motion, cf. [21, 25, 28];
- (4) My former Ph.D. student Shopple and I have developed a body-fitted finite-element level-set method. In particular, we have a new stable method to reinitialize a level-set function.

Some of these are summarized in the review article [24]. Currently, I am also developing a diffuse-interface approach to the variational solvation of molecules.

Publications

- [1] Bo Li, Superconvergence for higher-order triangular finite elements, *Mathematica Numerica Sinica*, 11(4), 413–417, 1989. Selected for republication: *Chinese J. Numer. Math. Appl.*, 12, 75–79, 1990.
Note: This paper is cited as “a little known but in my opinion important paper” in: L. B. Wahlbin, *Superconvergence in Galerkin Finite Element Methods*, Springer, 1995 (cf. Section 7.4).
- [2] Hongsen Chen and Bo Li, Superconvergence analysis and error expansion for the Wilson nonconforming finite element, *Numer. Math.*, 69, 125–140, 1994.
- [3] Petr Klouček, Bo Li, and Mitchell Luskin, Analysis of a class of nonconforming finite elements for crystalline microstructures, *Math. Comp.*, 65, 1111–1135, 1996.
- [4] Bo Li and Mitchell Luskin, Finite element analysis of microstructure for the cubic to tetragonal transformation, *SIAM J. Numer. Anal.*, 35, 376–392, 1998.
- [5] Bo Li and Mitchell Luskin, Nonconforming finite element approximation of crystalline microstructure, *Math. Comp.*, 67, 917–946, 1998.
- [6] Bo Li and Mitchell Luskin, Approximation of a martensitic laminate with varying volume fractions, *ESAIM: Math. Model. Numer. Anal.*, 33, 67–87, 1999.
- [7] Bo Li and Mitchell Luskin, Theory and computation for the microstructure near the interface between twinned layers and a pure variant of martensite, *Materials Sci. Eng. A*, 273, 237–240, 1999.
- [8] Bo Li and Zhimin Zhang, Analysis of a class of superconvergence patch recovery techniques for linear and bilinear finite elements, *Numer. Methods PDE*, 15(2), 151–167, 1999.
- [9] Kaushik Bhattacharya, Bo Li, and Mitchell B. Luskin, The simply laminated microstructure in martensitic crystals that undergo a cubic to orthorhombic phase transformation, *Arch. Rational Mech. Anal.*, 149, 123–154, 1999.
- [10] Bo Li, Approximation of martensitic microstructure with general homogeneous boundary data, *J. Math. Anal. Appl.*, 266, 451–467, 2002.
- [11] Russel E. Caflisch and Bo Li, Analysis of island dynamics in epitaxial growth of thin films, *SIAM Multiscale Model. Simul.*, 1, 150–171, 2003.
- [12] Bo Li, Finite element analysis of a class of stress-free martensitic microstructures, *Math. Comp.*,

- 72(244), 1675–1688, 2003.
- [13] Xingzhou Yang, Bo Li, and Zhilin Li, The immersed interface method for elasticity problems with interfaces, *Dyn. Contin. Discret Impuls. Syst. Ser. A: Math. Anal.*, 10, 783–808, 2003.
 - [14] Bo Li and Jian-Guo Liu, Thin film epitaxy with or without slope selection, *European J. Appl. Math.*, 14, 713–743, 2003.
 - [15] Bo Li, Lagrange interpolation and finite element superconvergence, *Numer. Methods PDE*, 20, 33–59, 2004.
 - [16] Eberhard Bänsch, Frank Hausser, Omar Lakkis, Bo Li, and Axel Voigt, Finite element method for epitaxial growth with attachment-detachment kinetics, *J. Comput. Phys.*, 194, 409–434, 2004.
 - [17] Bo Li, Andreas Rätz, and Axel Voigt, Stability of a circular epitaxial island, *Physica D*, 198, 231–247, 2004.
 - [18] Bo Li and Jian-Guo Liu, Epitaxial growth without slope selection: energetics, coarsening, and dynamic scaling, *J. Nonlinear Sci.*, 14, 429–451, 2004.
 - [19] Bo Li, Variational properties of unbounded order parameters, *SIAM J. Math. Anal.*, 38, 16–36, 2006.
 - [20] Bo Li, High-order surface relaxation vs. the Ehrlich–Schwoebel effect, *Nonlinearity*, 19, 2581–2603, 2006.
 - [21] Li-Tien Cheng, Joachim Dzubiella, J. Andrew McCammon, and Bo Li, Application of the level-set method to the implicit solvation of nonpolar molecules, *J. Chem. Phys.*, 127, 084503, 2007.
- Note:** This paper was selected for republication in *The Virtual J. of Nanoscale Sci. & Tech.*, Volume 16, Issue 10, 2007.
- [22] Yan Gong, Bo Li, and Zhilin Li, Immersed-interface finite-element method for elliptic interface problems with non-homogeneous jump conditions, *SIAM J. Numer. Anal.*, 46, 472–495, 2008.
 - [23] Jianwei Che, Joachim Dzubiella, Bo Li, and J. Andrew McCammon, Electrostatic free energy and its variations in implicit solvent models, *J. Phys. Chem. B*, 112, 3058–3069, 2008.
 - [24] Bo Li, John Lowengrub, Andreas Rätz, and Axel Voigt, Geometric evolution laws for thin crystalline films: modeling and numerics, Review Article, *Commun. Comput. Phys.*, 6, 433–482, 2009.
 - [25] Li-Tien Cheng, Yang Xie, Joachim Dzubiella, J. Andrew McCammon, Jianwei Che, and Bo Li, Coupling the level-set method with molecular mechanics for variational implicit solvation of nonpolar molecules, *J. Chem. Theory Comput.*, 5, 257–266, 2009.
 - [26] Bo Li, Minimization of electrostatic free energy and the Poisson–Boltzmann equation for molecular solvation with implicit solvent, *SIAM J. Math. Anal.*, 40, 2536–2566, 2009.
 - [27] Bo Li, Continuum electrostatics for ionic solutions with nonuniform ionic sizes, *Nonlinearity*, 22, 811–833, 2009.
- Note:** This article was selected for inclusion in the IOP (Institute of Physics) Select. Subject: Applied Mathematics and Mathematical Physics. From the IOP website: IOP select comprises “articles chosen by our Editors for their novelty, significance and potential impact on future research”, and “reflects both the breadth and international significance of papers published in our prestigious peer reviewed journals.”
- [28] Li-Tien Cheng, Zhongming Wang, Piotr Setny, Joachim Dzubiella, Bo Li, and J. Andrew McCammon, Interfaces and hydrophobic interactions in receptor-ligand systems: A level-set variational implicit solvent approach, *J. Chem. Phys.*, 131, 144102-1–144102-10, 2009.
 - [29] Piotr Setny, Zhongming Wang, Li-Tien Cheng, Bo Li, J. Andrew McCammon, and Joachim Dzubiella, Dewetting-controlled binding of ligands to hydrophobic pockets, *Phys. Rev. Lett.*, 103, 187801, 2009.
 - [30] Bo Li, Zhongming Wang, Benzhuo Lu, and J. Andrew McCammon, Solutions to a reduced Poisson–Nernst–Planck system and determination of reaction rates, 2009 (submitted).